

FTUV-10-1004
 KA-TP-30-2010
 SFB/CPP-10-88

Precise predictions for (non-standard) $W\gamma$ +jet production

F. Campanario^{a,*}, C. Englert^{a,b,†}, and M. Spannowsky^{c,‡}

^a Institute for Theoretical Physics, Karlsruhe Institute of Technology,
 76128 Karlsruhe, Germany

^b Institute for Theoretical Physics, Heidelberg University,
 69120 Heidelberg, Germany

^c Institute of Theoretical Science, University of Oregon,
 Eugene, OR 97403-5203, USA

Abstract

We report on a detailed investigation of the next-to-leading order (NLO) QCD corrections to $W\gamma$ +jet production at the Tevatron and the LHC using a fully-flexible parton-level Monte Carlo program. We include the full leptonic decay of the W , taking into account all off-shell and finite width effects, as well as non-standard $WW\gamma$ couplings. We find particularly sizable corrections for the currently allowed parameter range of anomalous couplings imposed by LEP data. In total the NLO differential distributions reveal a substantial phase space dependence of the corrections, leaving considerable sensitivity to anomalous couplings beyond scale uncertainty at large momentum transfers in the anomalous vertex.

*francam@particle.uni-karlsruhe.de

†c.englert@thphys.uni-heidelberg.de

‡mspannow@uoregon.edu

1 Introduction

Electroweak diboson production in association with a hard jet is an important class of processes at hadron colliders such as the Large Hadron Collider (LHC) or the Tevatron. Electroweak boson phenomenology generically provides a window to the electroweak symmetry breaking sector, and diboson signatures with or without jets are therefore potentially sensitive to new interactions beyond the Standard Model (BSM). Equally important, SM-diboson+jet production contributes to the irreducible background of new physics searches in these channels. Hence, precise cross section predictions are mandatory to obtain a correct interpretation of possible excesses, which might be observed in the near future. The total cross sections for the diboson+jet production processes are fairly large compared to the pure diboson production channels if extra jet emission at large available center-of-mass energy is kinematically unsuppressed. The large one jet-inclusive cross section is mainly due to accessing the (anti)proton's gluon parton distribution function at small momentum fractions already at leading order (LO). At the same time, the gluon-induced partonic subprocesses opening up at $\mathcal{O}(\alpha_s)$ give rise to exceptionally large next-to-leading order (NLO) QCD corrections to inclusive diboson production, see Ref. [1]. Qualitatively similar observations have also been made for the NLO QCD corrections to various diboson+jet production processes in a series of recent publications [2–9].

In the present paper we extend our NLO calculation of $p\bar{p}, pp \rightarrow W^\pm\gamma + \text{jet} + X$ [5] to anomalous $WW\gamma$ couplings*. We review the SM $W^\pm\gamma + \text{jet}$ phenomenology in detail and discuss its modifications due to anomalous couplings at NLO QCD precision. This allows us to discriminate between the effects of new physics in terms of effective interactions from the impact of higher order corrections. Anomalous couplings searches represent benchmark tests for non-SM interactions at the LHC at small integrated luminosity $\mathcal{L} \lesssim 30 \text{ fb}^{-1}$ (see, e.g., Ref. [10]). Measurement and discovery strategies have received lots of attention, both from the theoretical (e.g. Refs. [11–14]) and the experimental side (e.g. Refs. [10, 15–18]). In this context, diboson production processes are important channels at the LHC because they exhibit large total rates, and, in case of $W^\pm\gamma$ production, because they are sensitive to deviations of the underlying electroweak model from the SM via so-called radiation zeros. These classical zeros of the amplitude in the $q\bar{Q} \rightarrow W^\pm\gamma$ channels at the photon center-of-mass scattering angles $\cos\theta_\gamma = \mp 1/3$ are special to the completely destructive interference of gauge boson-radiation in an unbroken renormalizable field theory, Ref. [19]. Any deviation from QED by additional non-SM operators ultimately destroys this characteristic radiation pattern. At the LHC, the antiquark direction is, in principle, indistinguishable from the quark direction because of the proton-proton initial state, and the radiation zero gets considerably washed out. "Signing" the quark direction according to the event's overall boost, which has been considered in the context of dilepton asymmetries and electroweak mixing angle measurements [20], has been shown to efficiently lift the initial state's degeneracy in Ref. [10]. Furthermore, the radiation zero remains present only if additional electromagnetically neutral (e.g. gluonic) radiation is collinear to the photon. Hence, additional QCD

*For convenience we refer to the computed processes as $W^\pm\gamma + \text{jet}$ production even though we include all finite width and off-shell effects of the massive W .

emission, as part of the NLO contribution to $W\gamma$ production, is dangerous to observing the radiation zero. At the same time, the radiation zero becomes nearly impossible to measure in $W\gamma$ +jet production [13].

Crucial to significance-improving strategies [11] is therefore an additionally-imposed jet veto[†]. Jet vetoing, however, is a delicate strategy in fixed-order perturbation theory from a theoretical point of view. The observed reduction of scale dependence for the exclusive $W\gamma$ production at the LHC (see Ref. [1]) is predominantly due to excluding a region of phase space from the total inclusive cross section, which is well-accessible at the large available center-of-mass energy. This is also reflected in additional jet radiation becoming highly probable as part of the real emission contribution to the NLO diboson cross section, $\sigma(W\gamma + \text{jet})/\sigma(W\gamma) \sim 3$. Hence, the dominant perturbative uncertainties result from the $W\gamma + \text{jet}$ contribution, which is a leading order α_s contribution to NLO $W\gamma$ production. Consequently, current Monte Carlo-driven strategies that involve jet vetos to measure anomalous couplings from fits to high transverse momentum distributions (via e.g. neuronal net algorithms trained to the NLO $W\gamma$ distributions) inherit significant uncertainties, considerably larger than those given by scale variations of the exclusive NLO cross sections. By computing $W\gamma + \text{jet}$ production at NLO accuracy, we are able to realistically estimate the anomalous parameters' impact on the vetoed cross section and contribute a crucial part towards modelling inclusive $W\gamma$ production at a higher perturbative precision.

We organize this paper as follows: Section 2 gives details on our Monte Carlo implementation and introduces the notion of anomalous $WW\gamma$ couplings to the reader. In Sec. 3, we discuss the numerical results; we give total cross sections and differential distributions, both for SM and anomalous production. We also comment on the sensitivity to anomalous couplings in NLO QCD $W\gamma + \text{jet}$ production at the LHC and we quote $W\gamma + \text{jet}$ cross sections for selection cuts adapted to anomalous couplings' searches. The phenomenological impact of anomalous couplings on $W\gamma + \text{jet}$ production at the Tevatron is too small for parameter choices that are compatible with the bounds imposed by LEP data, Ref. [17]. Hence, we only quote Tevatron results for SM-like production in Sec. 3.3. Section 4 closes with a summary and gives an outlook to future work. Our Monte Carlo code will become publicly available with an upcoming update of VBFNLO [21].

2 Details of the calculation

There are three contributing partonic subprocesses at $\mathcal{O}(\alpha^3 \alpha_s)$ for $p\bar{p}, pp \rightarrow e^-\bar{\nu}_e \gamma j + X$,

$$q\bar{Q} \rightarrow \ell^-\bar{\nu}_\ell \gamma g, \tag{1a}$$

$$\bar{Q}g \rightarrow \ell^-\bar{\nu}_\ell \gamma \bar{q}, \tag{1b}$$

$$qg \rightarrow \ell^-\bar{\nu}_\ell \gamma Q, \tag{1c}$$

[†]The jet veto also removes kinematical configurations which are less sensitive to anomalous couplings due to small momentum transfers in the $WW\gamma$ vertex from the total cross section, see below.

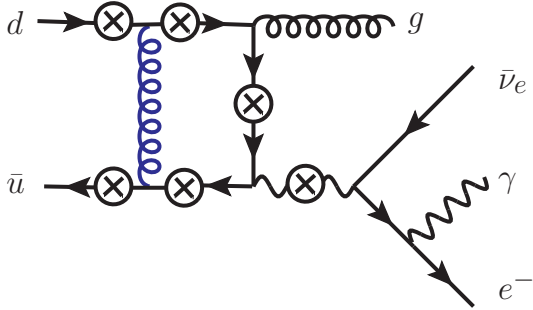


Figure 1: Representative Feynman graph contributing to the virtual corrections to the partonic subprocess $\bar{u}d \rightarrow e^- \bar{\nu}_e \gamma g$ at $\mathcal{O}(\alpha^3 \alpha_s^2)$. The crosses mark points where the photon can be attached to the quarks or the W for the fixed gluon- W order along the quark line.

not counting the subprocesses, which follow from interchanging the beam directions. We use the shorthand notation $q = (d, s)$ and $Q = (u, c)$ and assume a diagonal CKM matrix. At the LHC, a non-diagonal CKM matrix decreases our leading order results only at the per mil-level. Unitarity of the (non-diagonal) CKM matrix guarantees that all CKM-dependence drops out for flavor-blind observables computed from the dominant gluon-induced subprocesses. At the Tevatron, we find our cross sections decreased by about 3%. Both modifications are smaller than the residual scale dependence at NLO, so that a diagonal CKM matrix is an adequate approximation for our purposes. Bottom quark contributions are absent at LO for the above approximations and can be further suppressed experimentally by b vetoing, and we therefore neglect bottom contributions throughout the computation.

The LO matrix elements of Eq. (1) are calculated using HELAS routines [22] generated with MADGRAPH [23]. Although we refer to the processes as $W^\pm \gamma + \text{jet}$ production for convenience, we include all off-shell and finite width effects of the W 's decay to leptons, as well as the photon's coupling to the charged final state lepton and calculate the full QCD corrections to the processes $pp, p\bar{p} \rightarrow \ell^- \bar{\nu}_\ell \gamma j + X$ and $pp, p\bar{p} \rightarrow \ell^+ \nu_\ell \gamma j + X$ at $\mathcal{O}(\alpha^3 \alpha_s^2)$. Representative virtual Feynman graph topologies are sketched in Fig. 1. We perform the numerical phase space integration with a modified version of VEGAS [24], which is part of the VBFNLO package. We divided up the integration and explicitly sum over different channels that are optimized for the two and three-body decay of the (off-shell) W boson, $pp, p\bar{p} \rightarrow W\gamma j \rightarrow \ell\nu\gamma j$ and $pp, p\bar{p} \rightarrow Wj \rightarrow \ell\nu\gamma j$, respectively. For additional details on the phase space integration's validation against MADEVENT [23] and SHERPA [25], we refer the reader to our previous publication [5]. The numerical implementation includes the finite width of the W by using the fixed width scheme[‡] of Ref. [26]: The weak mixing angle is taken to be real and we use Breit-Wigner propagators for the massive W throughout.

The counter term-renormalized virtual amplitude for, e.g., $\bar{u}d \rightarrow \ell^- \bar{\nu}_e \gamma g$ (Fig. 1) in

[‡]This is also the width scheme used by MADGRAPH.

conventional dimensional regularization $d = 4 - 2\varepsilon$ can be cast into the form,

$$\begin{aligned} \mathcal{M}_{\text{Virt+CT}}^{\text{1-Loop}} = & \frac{\alpha_s(\mu_R^2)}{4\pi} \frac{\mathcal{M}_{\text{LO}}}{\Gamma(1-\varepsilon)} \left[\frac{1}{2} \left\{ \left(\frac{4\pi\mu_R^2}{-u} \right)^\varepsilon + \left(\frac{4\pi\mu_R^2}{-t} \right)^\varepsilon \right\} \left(-\frac{C_A}{\varepsilon^2} - \frac{\gamma_g}{\varepsilon} \right) \right. \\ & + \frac{C_A}{2C_F} \left\{ \left(\frac{4\pi\mu_R^2}{-u} \right)^\varepsilon + \left(\frac{4\pi\mu_R^2}{-t} \right)^\varepsilon - 2 \left(\frac{4\pi\mu_R^2}{-s} \right)^\varepsilon \right\} \left(-\frac{C_F}{\varepsilon^2} - \frac{\gamma_q}{\varepsilon} \right) \\ & \left. + 2 \left(\frac{4\pi\mu_R^2}{-s} \right)^\varepsilon \left(-\frac{C_F}{\varepsilon^2} - \frac{\gamma_q}{\varepsilon} \right) \right] + \widetilde{\mathcal{M}}_{\text{Virt}}(-s, -t, -u), \end{aligned} \quad (2)$$

with $C_F = 4/3$ and $C_A = 3$ denoting the casimirs of the fundamental and adjoint representations, respectively. The virtual amplitude exhibits an identical structure in color space as the Born matrix element and we implicitly assume the $\mathfrak{su}(3)$ generator in the fundamental representation to be part of the definitions of \mathcal{M}_{LO} and $\widetilde{\mathcal{M}}_{\text{Virt}}$. The constants γ_i are fixed by the $SU(3)$ representations of the $N_F = 5$ active quark flavors and the gluons,

$$\gamma_q = \gamma_{\bar{q}} = \frac{3}{2}C_F, \quad \gamma_g = \frac{11}{6}C_A - \frac{2}{3}T_r N_F, \quad (3)$$

where $T_r = 1/2$ is the Dynkin index of the fundamental representation. s, t, u denote the familiar Mandelstam variables of a $2 \rightarrow 2$ process, taken to be space-like. Depending on the subprocess, the analytical continuation to physical kinematics is performed automatically within our numerical code by effectively restoring the propagators' ε description. To arrive at the correct logarithms when evaluating Eq. (2) for physical s, t, u , we have to write, e.g.,

$$\log(-s) = \log(|s|) - i\pi\Theta(-s) \quad (4)$$

for the $q\bar{Q}$ induced subprocesses for which s is a time-like quantity. Similar formulae have to be taken into account for the analytical continuation of the dilogarithms and can be inferred from the literature, e.g. from Ref. [27], appendix C. $\widetilde{\mathcal{M}}_{\text{Virt}}$ in Eq. (2) represents finite contributions that embrace tensor coefficients and fermion chains after algebraic manipulations. We also implicitly include the so-called rational terms to our definition of $\widetilde{\mathcal{M}}_{\text{Virt}}$. These finite contributions arise from the interplay of d -dimensional numerator and denominator algebra in the limit $\varepsilon \rightarrow 0$ (see, e.g., [28]). To compute the tensor coefficients, we apply the Passarino-Veltman recursion up to box topologies [29] and the Denner-Dittmaier reduction for pentagon graphs [30].

The full virtual amplitude can be assembled from elementary building blocks, that divide the one loop graphs into certain groups. This strategy has already been applied to calculate a series of different processes at NLO QCD precision in Ref. [31], both in the SM and beyond. Concretely, we sum all self-energy, triangle, box and pentagon corrections to a quark line with three attached gauge bosons of a given order to yield a single numerical routine. A similar routine is constructed from a quark line with two attached gauge bosons (see Fig. 1). These routines are set up with an in-house framework that partly uses FEYNARTS [32] and FEYNCALC [33]. From these building blocks we construct the full SM loop amplitude for a given subprocess by trivial permutations of the bosons' momenta and polarization vectors, which also encode the two and three-body decay of the massive W depending on the building block. Replacing the SM polarization vectors by polarization vectors modified by

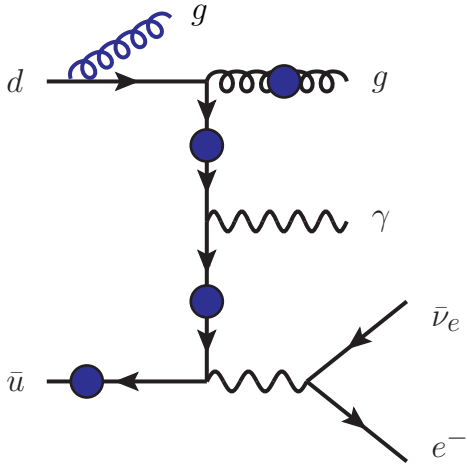


Figure 2: Sample Feynman graph contributing to the partonic real emission subprocess $\bar{u}d \rightarrow e^- \bar{\nu}_e \gamma gg$ at $\mathcal{O}(\alpha^3 \alpha_s^2)$. The gluon can also be attached to the quark and gluon lines at the positions marked by the circles. Feynman graph topologies, where the photon is radiated off at different positions analogous to Fig. 1, are not shown.

including anomalous $WW\gamma$ couplings, we straightforwardly generalize our NLO calculation to anomalous $W\gamma +$ jet production. The renormalization in Eq. (2) is performed on-shell for the wave functions and we use the $\overline{\text{MS}}$ -scheme to renormalize the strong coupling constant. The virtual corrections to all other subprocesses of Eq. (1) can be recovered from Eq. (2) by crossing and analytical continuation analogous to Eq. (4).

To speed up the numerical evaluation of the 90 subprocesses of the real emission contribution, we compute the respective matrix elements using optimized code that employs the spinor helicity formalism of Ref. [34]. The generalization to matrix elements with anomalous couplings is again performed by modifying the three-body effective W polarization vector to include the non-SM interactions of Sec. 2.1. The subprocesses for $pp, p\bar{p} \rightarrow e^- \bar{\nu}_e \gamma jj + X$ at $\mathcal{O}(\alpha^3 \alpha_s^2)$ can be classified, modulo crossing, flavor summation, and initial state interchange, into

$$\bar{u}u \rightarrow \ell^- \bar{\nu}_\ell \gamma \bar{d}u, \quad \bar{u}u \rightarrow \ell^- \bar{\nu}_\ell \gamma \bar{s}c, \quad (5a)$$

$$\bar{d}d \rightarrow \ell^- \bar{\nu}_\ell \gamma \bar{u}d, \quad \bar{d}d \rightarrow \ell^- \bar{\nu}_\ell \gamma \bar{c}s, \quad (5b)$$

$$\bar{u}d \rightarrow \ell^- \bar{\nu}_\ell \gamma gg. \quad (5c)$$

Representative Feynman topologies for the last line's subprocess are indicated in Fig. 2. We store intermediate numerical results common to all subprocesses and reuse them whenever possible to speed up the numerical implementation. All matrix elements have been checked explicitly against code generated with **MADGRAPH** as well as against **SHERPA** for integrated cross sections (cf. [5]). Applying the dipole subtraction of Catani and Seymour [35], we have verified our implementation against code generated with the **MADDIPOLES** [36] package. Our code is optimized such that intermediate dipole results are reused in order to avoid redundant dipole or Born-level matrix element calculations. We also recycle the dipoles' Born-level matrix elements into the integration of the finite collinear remainder, which is left after renormalization of the parton distribution functions [35, 38]. We integrate this contribution over the real emission phase space applying the phase space mappings of Ref. [39]. The remaining IR-singularities of the virtual matrix element Eq. (2) cancel analytically against the one-parton phase space-integrated dipoles, symbolically denoted by $\langle \mathbf{I} \rangle$ in the language

of Ref. [35]. For, e.g., the $\bar{q}Q$ -induced channels adding the $\langle \mathbf{I} \rangle$ operator yields

$$\begin{aligned}
2 \operatorname{Re} \left(\mathcal{M}_{\text{Virt+CT}}^{1\text{-Loop}, q\bar{Q} \rightarrow g} \left[\mathcal{M}_{\text{LO}}^{q\bar{Q} \rightarrow g} \right]^* \right) + \langle \mathbf{I} \rangle = & \frac{\alpha_s(\mu_R^2)}{2\pi} \frac{|\mathcal{M}_{\text{LO}}^{q\bar{Q} \rightarrow g}|^2}{\Gamma(1-\varepsilon)} \\
& \times \left[\frac{1}{2} \left\{ \left(\frac{4\pi\mu_R^2}{-t} \right)^\varepsilon + \left(\frac{4\pi\mu_R^2}{-u} \right)^\varepsilon \right\} \left(K_g + \gamma_g - \frac{\pi^2 C_A}{3} \right) - \left(K_q + \gamma_q - \frac{\pi^2 C_F}{3} \right) \right. \\
& \times \left. \left\{ \frac{C_A - 2C_F}{C_F} \left(\frac{4\pi\mu_R^2}{s} \right)^\varepsilon - \frac{C_A}{2C_F} \left(\frac{4\pi\mu_R^2}{-t} \right)^\varepsilon - \frac{C_A}{2C_F} \left(\frac{4\pi\mu_R^2}{-u} \right)^\varepsilon \right\} \right] \\
& + 2 \operatorname{Re} \left(\widetilde{\mathcal{M}}_{\text{Virt}}' \left[\mathcal{M}_{\text{LO}}^{q\bar{Q} \rightarrow g} \right]^* \right), \quad (6)
\end{aligned}$$

with

$$K_q = K_{\bar{q}} = \left(\frac{7}{2} - \frac{\pi^2}{6} \right) C_F, \quad K_g = \left(\frac{67}{18} - \frac{\pi^2}{6} \right) C_A - \frac{10}{9} T_r N_F, \quad (7)$$

where we have already performed the analytical continuation to time-like s . The primed $\widetilde{\mathcal{M}}_{\text{Virt}}'$ in Eq. (6) indicates that we deal with a changed finite piece compared to Eq. (2) due to the analytic continuation. Note that we again include the Born level color structure into the definitions of the amplitudes; summing and averaging over colors and spins yields trivial subprocess-dependent additional prefactors. Equation (6) is explicitly free of IR divergencies and hence finite for $\varepsilon \rightarrow 0$. A similar factorization and cancellation up to box diagrams has been demonstrated in Ref. [40].

2.1 Anomalous $WW\gamma$ couplings

We parametrize deviations of the SM electroweak sector by extending the SM Lagrangian by the most general, QED-preserving, Lorentz and \mathcal{CP} -invariant operators up to dimension six [41],

$$\mathcal{L}_{WW\gamma} = -ie \left[W_{\mu\nu}^\dagger W^\mu A^\nu - W_\mu^\dagger A_\nu W^{\mu\nu} + \kappa W_\mu^\dagger W_\nu F^{\mu\nu} + \frac{\lambda}{m_W^2} W_{\lambda\mu}^\dagger W_\nu^\mu F^{\nu\lambda} \right]. \quad (8)$$

It is customary to express the κ -induced deviation from the SM operators[§] by $\Delta\kappa = \kappa - 1$. The parameters $\Delta\kappa$ and λ are related to the electric quadrupole moment Q_W and magnetic dipole moment μ_W of the W boson [41],

$$\mu_W = \frac{e}{2m_W} (2 + \Delta\kappa + \lambda), \quad Q_W = -\frac{e}{m_W^2} (1 + \Delta\kappa - \lambda). \quad (9)$$

Retaining unitarity at high energies is crucial to meaningfully modeling physics beyond the SM. On the one hand, if probability conservation is violated, the cross section receives a sizable contribution from probing the matrix elements at large invariant masses, even though the parton luminosities tame the matrix elements' unphysical growth in this particular phase

[§]We recover the electroweak part of the SM by choosing the parameters $\kappa = 1$ and $\lambda = 0$.

space region. On the other hand, if unitarity is conserved, the phenomenology is mainly dominated by comparatively low invariant masses by the same reason. In order not to violate unitarity, the parameters $\Delta\kappa$ and λ have to be understood as low-energy form factors, and their precise momentum dependence does depend sensitively on physics beyond the SM. However, a widely-used phenomenological parametrization is (cf. Refs. [11, 41]),

$$\Delta\kappa = \frac{\Delta\kappa_0}{(1 + (p_\gamma + p_W)^2/\Lambda^2)^{n_\kappa}}, \quad \lambda = \frac{\lambda_0}{(1 + (p_\gamma + p_W)^2/\Lambda^2)^{n_\lambda}}, \quad (10)$$

where Λ represents the scale at which the beyond-the-SM interactions become strong, i.e. the scale at which W compositeness is resolved. p_γ and p_W denote the final state momenta of the photon and the W , respectively. Unitarity imposes $n_\kappa > 1/2$ and $n_\lambda > 1$ [42]; customary choices by experimentalists are dipole profiles $n_\kappa = n_\lambda = 2$ [10, 15–18]. Note that we do not include anomalous \mathcal{CP} -violating operators since they have already been tightly constrained by measurements of the neutron electric dipole moment [11, 43].

We include the anomalous interactions by constructing purpose-built HELAS routines that implement the effective Lagrangian of Eq. (8) in a straightforward way using **FEYNRULES** (Ref. [44]) to arrive at the analytical expression for the anomalous vertex function.

3 Numerical results

3.1 Selection criteria, general Monte Carlo input and photon isolation

Throughout, we use CTEQ6M parton distributions [45] with $\alpha_s(m_Z) = 0.118$ at NLO, and the CTEQ6L1 set at LO. We choose $m_Z = 91.188$ GeV, $m_W = 80.419$ GeV and $G_F = 1.16639 \times 10^{-5}$ GeV $^{-2}$ as electroweak input parameters and derive the electromagnetic coupling α and the weak mixing angle from SM-tree level relations. The center-of-mass energy is fixed to 14 TeV for LHC and to 1.96 TeV for Tevatron collisions. We consider one family of light leptons in the final state, which we treat as massless, i.e. we quote results for $pp, p\bar{p} \rightarrow e^-\bar{\nu}_e \gamma j + X$ or $pp, p\bar{p} \rightarrow \mu^-\bar{\mu}_e \gamma j + X$ when we speak of $W^-\gamma +$ jet production.

Jets are recombined from partons with pseudorapidity $|\eta| \leq 5$ applying the algorithm of Ref. [46] with resolution parameter $D = 0.7$. The reconstructed jets are required to lie in the rapidity range

$$|y_j| \leq 4.5. \quad (11)$$

The charged lepton and the photon are required to fall into the rapidity coverage of the electromagnetic calorimeter, i.e. we impose

$$|\eta_\ell| \leq 2.5, \quad |\eta_\gamma| \leq 2.5. \quad (12)$$

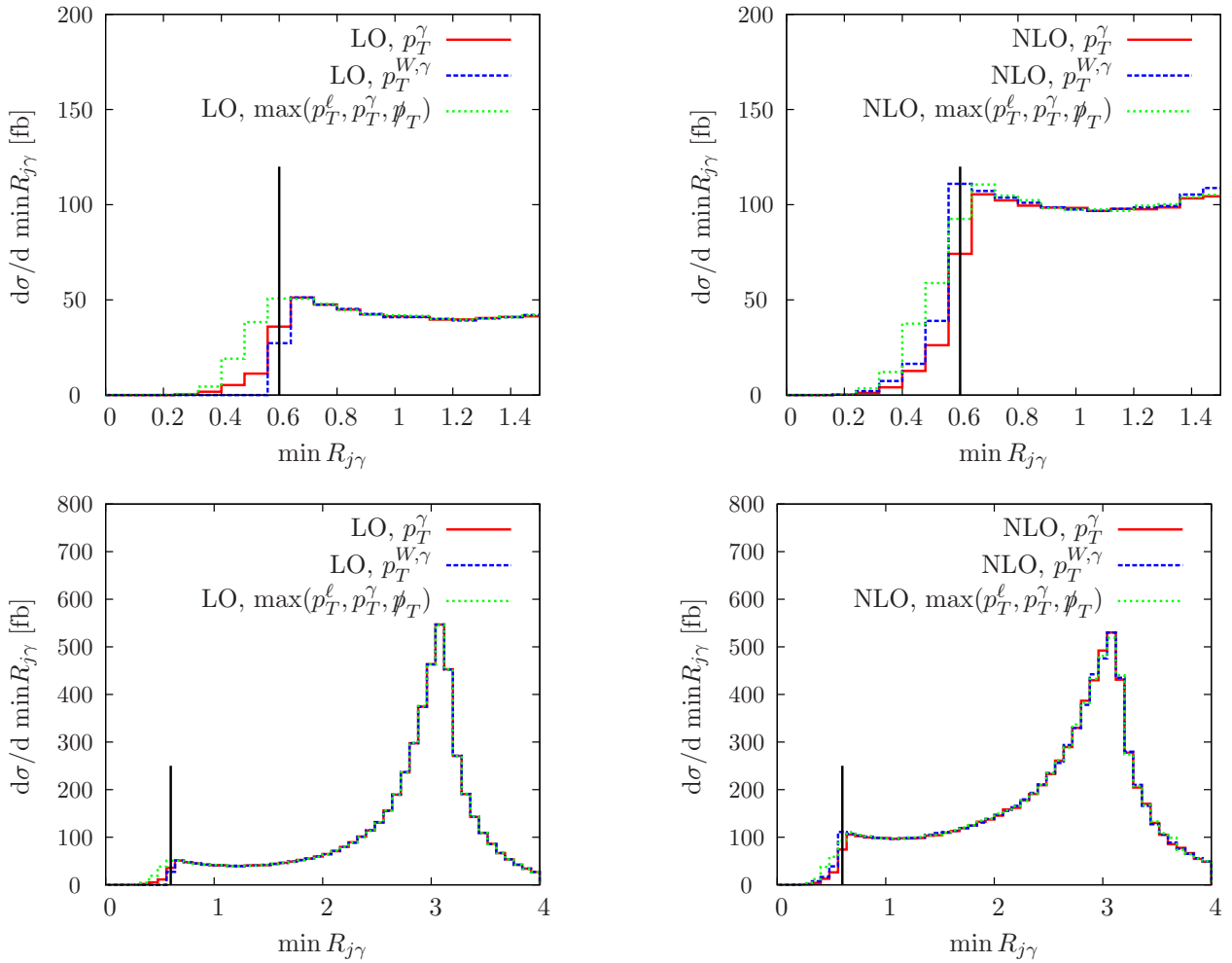


Figure 3: Minimal photon-jet separation in the azimuthal angle – pseudorapidity plane for $W^- \gamma + \text{jet}$ production at the LHC. Plotted are the leading order and next-to-leading order distributions for different isolation scales $\mathcal{E} = p_T^\gamma, p_T^{W,\gamma}, \max(p_T^\ell, p_T^\gamma, p_T)$ in Eq. (13). The upper row displays the lower row’s $\min R_{j\gamma}$ distributions around the isolation cone in more detail. The isolation parameter is $\delta_0 = 0.6$ (indicated by the vertical line), and $\mu_F = \mu_R = 100$ GeV. Cuts are chosen as described in the text.

In order not to spoil the cancellation of the IR singularities and to minimize contributions from non-perturbative jet fragmentation associated with collinear photon-jet configurations, we apply the photon isolation criterion of Ref. [47]:

$$\sum_{i, R_{i\gamma} < R} p_T^{\text{parton},i} \leq \frac{1 - \cos R}{1 - \cos \delta_0} p_T^\gamma \quad \forall R \leq \delta_0. \quad (13)$$

The index i in Eq. (13) runs over all partons found in a cone around the photon of size R in the azimuthal angle–pseudorapidity plane. The IR-safe cone size around the photon is given by δ_0 , and, in principle, p_T^γ can be replaced by an arbitrary energy scale \mathcal{E} , which then determines the penetrability of the photon cone by soft QCD radiation.

In a realistic experimental setting, the photon identification efficiency depends on the

number of finite-sized calorimeter towers that enter the candidate photon reconstruction (cf. Ref. [48]). It is therefore worthwhile to note that the isolation scale choice implicitly enters in the photon definition and different scale choices will be accompanied by different identification efficiencies for small values of δ_0 . A detailed investigation of this direction should include effects ranging from pile-up and underlying event to NLO-corrected jet fragmentation and is beyond the scope of this work. For values of δ_0 much larger than the electromagnetic calorimeter cell size of $\Delta R \approx 0.04$, however, Eq. (13) is a “sliding-cut” prescription, which is experimentally well-defined on the level of already reconstructed particles. We can therefore compare the impact of the IR-safe isolation criterion to the NLO scale uncertainty, which turns out to be of order 10%. Replacing p_T^γ in Eq. (13) by other intrinsic scales to the process, e.g. by $\max p_T^j$, corrects our NLO results at the level of 1% for inclusive cuts and $\delta_0 = 0.6$ (Fig. 3). Comparing the LO and NLO inclusive distributions we find a large net increase of the differential cross section. The differences in the choice of the isolation scale, however, are only visible in the jet-photon separation distribution around the photon cone $\min R_{j\gamma} \approx \delta_0$. For larger separations $\min R_{j\gamma} > \delta_0$ we do not find any notable phenomenological impact of the isolation scale once we take into account the cross section’s residual scale dependence on μ_R, μ_F . For the isolation scale $\mathcal{E} = p_T^{W,\gamma} = |\mathbf{p}_T^\gamma + \mathbf{p}_T^\ell + \cancel{\mathbf{p}}_T|$ the threshold behavior around δ_0 changes most significantly when comparing LO and NLO distributions (we denote the neutrino’s four-momentum by $\cancel{\mathbf{p}}$ in the following). The behaviour at LO is a consequence of $p_T^{W,\gamma} = p_T^j$ and the W recoiling against the photon-jet pair if the jet is emitted around the photon cone. Therefore, probing smaller parton-photon separations effectively means increasing the transverse momentum of the W for central events. The isolation scale, however, is set by the jet itself. Due to the exponential drop-off of the $p_T^W = |\mathbf{p}_T^\ell + \cancel{\mathbf{p}}_T|$ spectrum, collinear jet-photon configurations are highly attenuated for separations smaller than δ_0 at LO, see Fig. 3. At NLO the kinematical LO correlation of the jet and $W\gamma$ -system is modified by additional parton emission, which allows the W to be emitted at smaller transverse momenta. Thus, QCD radiation into the photon cone around the threshold δ_0 becomes more probable than at LO. At the same time, however, $p_T^{W,\gamma}$ decreases and more partons get vetoed at distances smaller than δ_0 , and a steep drop-off is still visible in $\min R_{j\gamma}$ around δ_0 at NLO for $\mathcal{E} = p_T^{W,\gamma}$ in Fig. 3. In addition, we add events with a positive-definite weight to the minimum-separation distribution with the second resolved jet approximately balancing the jet-photon- W system in p_T , which also modifies the $\min R_{j\gamma}$ threshold behaviour.

We now move on to investigate the general features of $W\gamma +$ jet production with inclusive cuts on jets, photon, and lepton; we require

$$p_T^j \geq 50 \text{ GeV}, \quad p_T^\ell \geq 20 \text{ GeV}, \quad p_T^\gamma \geq 20 \text{ GeV}. \quad (14)$$

To avoid the collinear photon-lepton configurations we impose a finite separation in the azimuthal angle-pseudorapidity plane of

$$R_{\ell\gamma} = \sqrt{\Delta\phi_{\ell\gamma}^2 + \Delta\eta_{\ell\gamma}^2} \geq 0.2. \quad (15)$$

For the jet-lepton separation we choose

$$R_{j\ell} \geq 0.2, \quad (16)$$

and for the photon isolation we impose

$$\delta_0 = 0.6. \quad (17)$$

It is customary to also analyze the cross sections' behavior with an additional 'no resolvable 2nd jet'–criterion [2], i.e. a veto on the second jet, if it gets resolved,

$$p_T^{j,\text{veto}} \geq 50 \text{ GeV}, \quad |y_j^{\text{veto}}| \leq 4.5 \quad (\text{exclusive NLO}). \quad (18)$$

This allows us to identify the dominant contributions to the NLO-inclusive cross section. In addition, it was shown in Ref. [5] that this cut leads to seemingly stable exclusive $W\gamma+\text{jet}$ production cross sections at the LHC. Similar observations have been made for the other diboson+jet cross sections provided in Refs. [2–4, 6–8]. The stabilization of the exclusive cross section does, however, not provide a reliable estimate of the perturbative cross sections' uncertainties over the whole phase space. We will discuss this in more detail in Sec. 3.2.

3.2 NLO QCD $W\gamma+\text{jet}$ production in the SM at the LHC

We quote the inclusive cross sections at the LHC for the chosen cuts in Tab. 1. The differences comparing W^+ to W^- is mainly due to the different parton distributions at the LHC. The cross sections' scale dependencies, estimated by varying $\mu_F = \mu_R$ by a factor two around 100 GeV, is reduced from approximately 11% to 7% when including the NLO QCD corrections. As already pointed out, introducing a veto on the second resolved jet, leads to considerable stabilization of the integrated NLO cross section; the one jet-exclusive cross sections (Tab. 2) exhibit scale variations of 0.5% for $W^-\gamma+\text{jet}$ and 2% for $W^+\gamma+\text{jet}$ production, respectively. Naively, this suggests that vetoing the second hard jet amounts to a perturbative stabilization of the NLO cross section at a lower exclusive rate by effectively rejecting the μ_R -dependence of the real emission dijet contributions to the hadronic NLO $W\gamma+\text{jet}$ cross sections. However, given that extra jet radiation becomes important in the tails of the transverse momentum distributions, Fig. 4, the veto introduces substantial uncertainties in this very phase space region. This can be inferred from Fig. 5, where we exemplarily examine the impact of the fixed-scale variation $\mu_F = \mu_R = 50 \text{ GeV}, \dots, 200 \text{ GeV}$ on the photon's transverse momentum for both inclusive and exclusive production. For completeness we note that dynamical scale choices, such as $\mu_R = \mu_F = \max p_T^j$, result in quantitatively similar uncertainty bands. While the distribution's uncertainty band's relative size is uniform over the entire range of the distribution for inclusive production, the jet

	$\sigma_{\text{incl}}^{\text{NLO}} \text{ [fb]}$	$K = \sigma_{\text{incl}}^{\text{NLO}} / \sigma^{\text{LO}}$
$W^-\gamma j$	615.3 ± 2.8	1.49
$W^+\gamma j$	736.5 ± 3.5	1.41

Table 1: Inclusive next-to-leading order cross sections and total K factors for the processes $pp \rightarrow e^+\nu_e\gamma j + X$ and $pp \rightarrow e^-\bar{\nu}_e\gamma j + X$ at the LHC for identified renormalization and factorization scales, $\mu_R = \mu_F = 100 \text{ GeV}$. The cuts are chosen as described in the text.

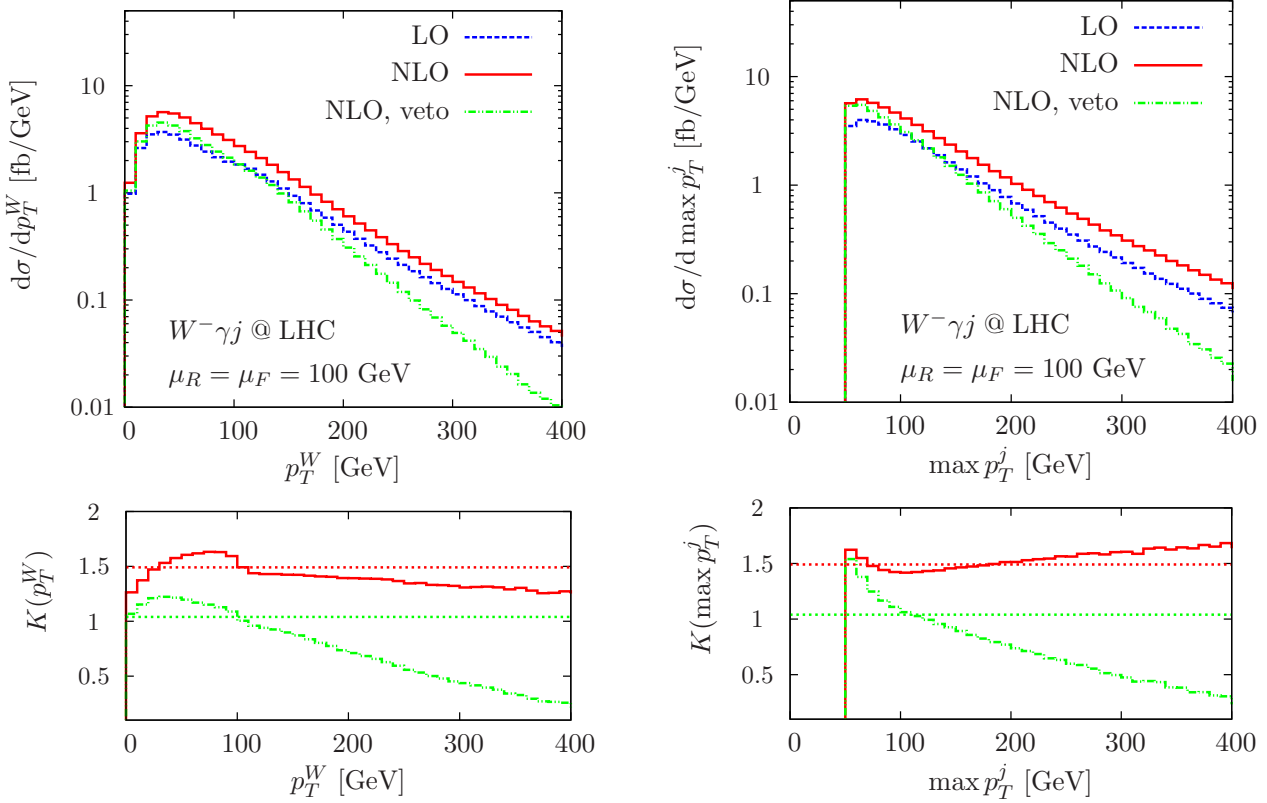


Figure 4: Transverse momentum of the W and maximum jet transverse momentum at leading order (dashed) and next-to-leading order (solid). The lower panels display the differential K factor, with the K factors of the total inclusive and exclusive production plotted as dashed horizontal lines. The W momentum is reconstructed from its decay products in the transverse plane.

	$\sigma_{\text{excl}}^{\text{NLO}}$ [fb]	$K = \sigma_{\text{excl}}^{\text{NLO}} / \sigma^{\text{LO}}$
$W^- \gamma j$	429.2 ± 0.8	1.04
$W^+ \gamma j$	495.1 ± 1.0	1.06

Table 2: Exclusive next-to-leading order cross sections and total K factors for the processes $pp \rightarrow e^+ \nu_e \gamma j + X$ and $pp \rightarrow e^- \bar{\nu}_e \gamma j + X$ at the LHC for identified renormalization and factorization scales, $\mu_R = \mu_F = 100$ GeV. The cuts are chosen as described in the text.

veto stabilizes $d\sigma_{\text{excl}}^{\text{NLO}}/dp_T^\gamma$ exclusively in threshold region, which dominates the integrated exclusive rate. In fact, the distributions for $\mu = 50$ GeV and $\mu = 100$ GeV, which are used to generate the uncertainty band in Fig. 5, intersect at $p_T^\gamma \approx 100$ GeV signaling an accidental cancellation of the renormalization and factorization scale dependence for the small total K factors of the exclusive sample. The large uncertainty in the exclusive p_T^γ distribution's tail then translates into an only mild overall scale dependence $\sigma_{\text{excl}}^{\text{NLO}}$. Similar conclusions have been drawn for $WZ + \text{jet}$ production in Ref. [8].

This is yet another example of the well-known fact that total K factors and total scale

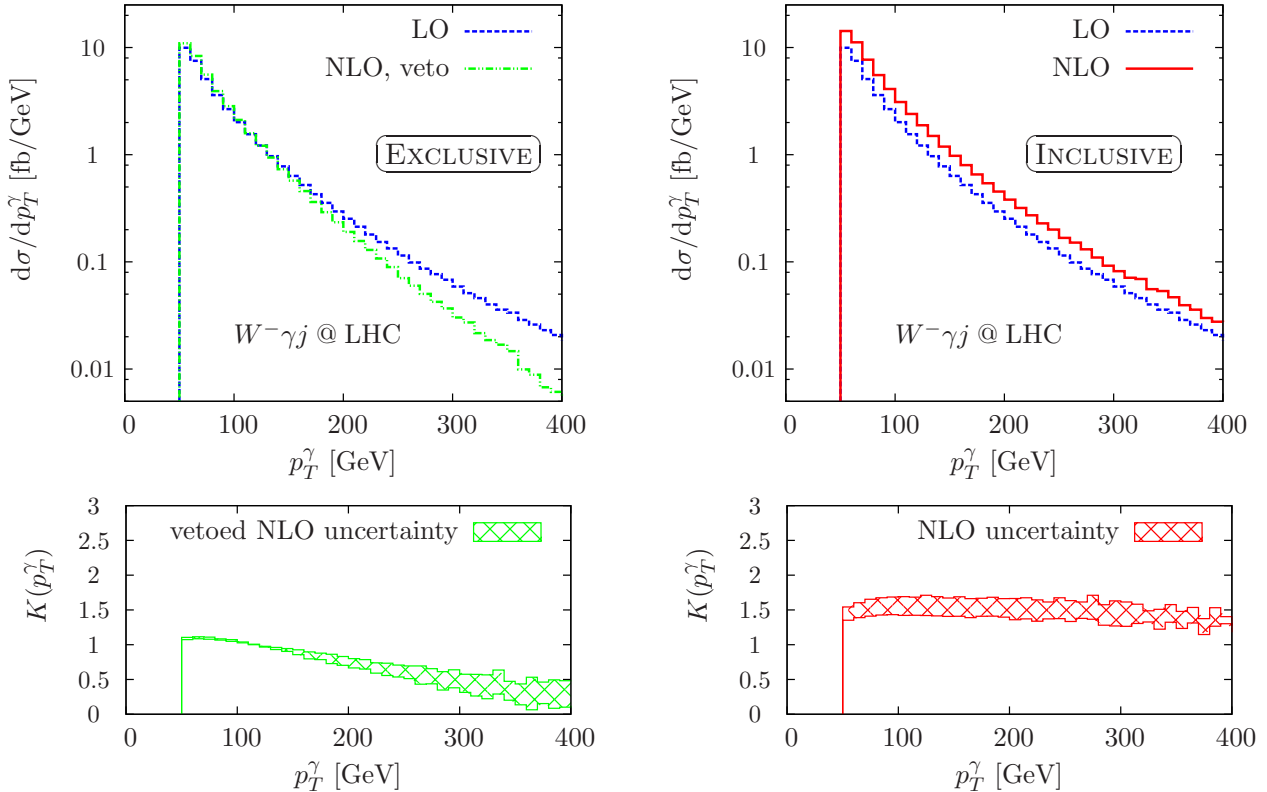


Figure 5: Transverse momentum of the photon for exclusive (left panel) and inclusive $W^- \gamma + \text{jet}$ production (right panel). The uncertainty bands refer to fixed scale variations around $\mu_R = \mu_F = 100$ GeV by a factor two in the NLO computation only.

variations tend to be misleading when quantifying the impact of QCD quantum corrections to a given process. A better understanding of the QCD effects can be gained from differential K factors of (IR-safe) observables \mathcal{O} ,

$$K(\mathcal{O}) = \frac{d\sigma^{\text{NLO}}}{d\mathcal{O}} \Big/ \frac{d\sigma^{\text{LO}}}{d\mathcal{O}}, \quad (19)$$

which encode the phase space dependence of the corrections, projected onto the respective observable. With unsuppressed extra jet radiation at the LHC's large center-of-mass energy[¶], the distributions' shapes are highly altered when including NLO inclusive corrections. While the shapes of purely electroweak distributions, i.e. distributions of observables that involve only photon, lepton and missing energy, survive to NLO QCD for the most part of the phase space, semi-hadronic observables get significantly modified with respect to their LO approximations due to additional jet radiation. Representatively, we show the azimuthal angle–pseudorapidity separation of lepton and photon and the minimal distance between jet and lepton in Fig. 6. We also plot the azimuthal angle between lepton and photon and

[¶]The proton is probed at small momentum fractions $x \sim 0.02$ at LO, which results in $\sigma^{\text{LO}}(W^\pm \gamma j) / \sigma^{\text{LO}}(W^\pm \gamma jj) \sim 2$ for the chosen selection criteria. Note that this is qualitatively different from the situation encountered in NLO $W\gamma$ production.

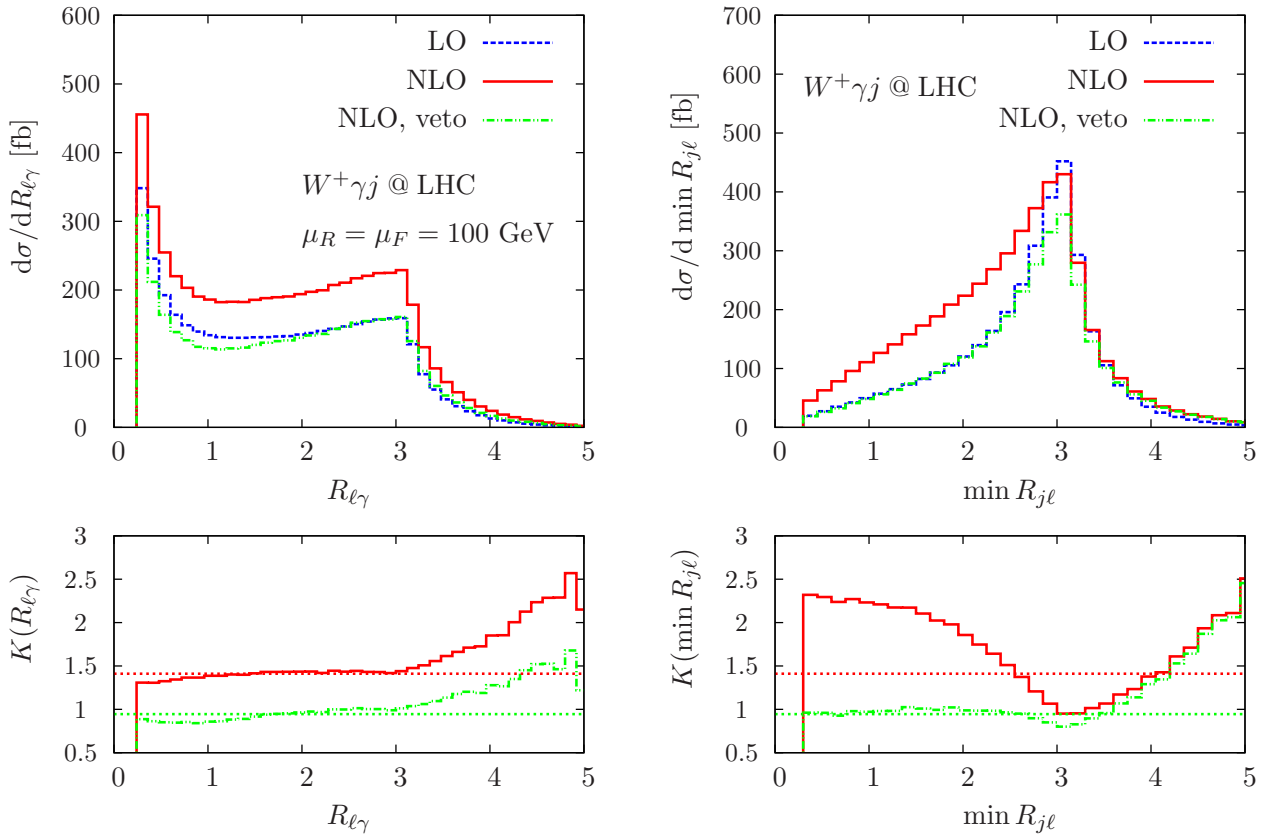


Figure 6: Lepton-photon separation and minimum jet-photon separation at LO and NLO. The horizontal lines display the K factors of the total inclusive and exclusive production.

W and photon in Fig. 8. The purely leptonic observables also receive sizable modifications at the edges of the phase space, which are determined by the chosen cuts. If, e.g., the $W\gamma$ system recoils against additionally emitted partons at NLO, the W and the photon are forced to larger rapidity differences (Fig. 7), which communicates to the azimuthal angle–pseudorapidity separation of lepton and photon at large values. Obviously this effect cannot be buffered by the additional jet veto. It is important to note that the pseudorapidity difference of the W and the photon in Fig. 7 is experimentally not observable because the neutrino’s longitudinal momentum explicitly enters the observable’s definition. We show the distribution for comparison only. All other observables do depend only on the missing transverse momentum, which is experimentally reconstructed from the event’s calorimeter entries [37].

The typical signatures of $W\gamma$ +jet production at the LHC are dominated by configurations close to the p_T -thresholds; the entire event is central with lepton and photon preferably emitted at small angular distances in the transverse plane. The collinear photon-lepton singularity is cut away by the requirement of Eq. (15). The photon is typically emitted collinear to the W in the transverse plane. The jet recoils against the $W\gamma$ pair, and is back-to-back to the W and the photon in the azimuthal angle distribution. For events with W and γ back-to-back (e.g. $|\phi_{W\gamma}| \geq 150$ deg, where the inclusive NLO cross sections drops

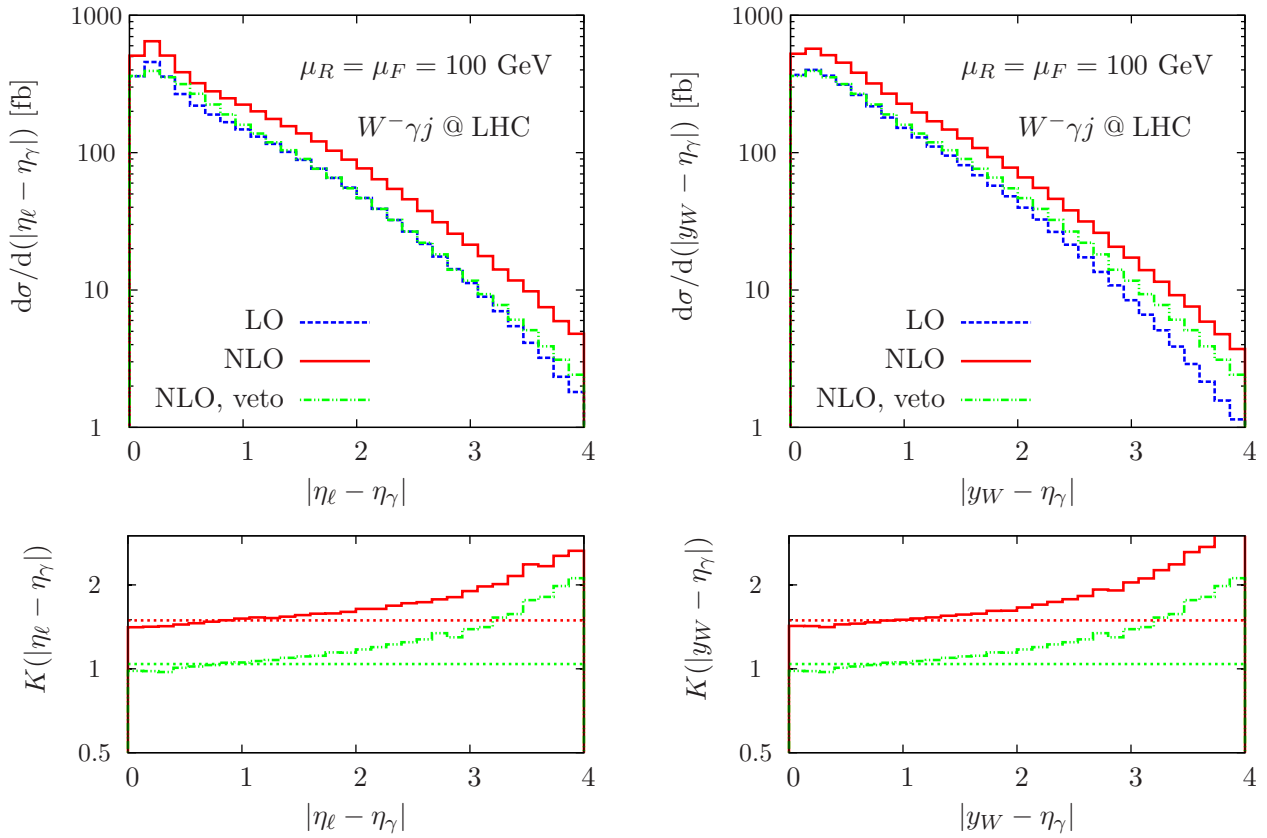


Figure 7: Lepton-photon and W -photon (pseudo)rapidity separation LO and NLO. The horizontal lines display the K factors of the total inclusive and exclusive production. The W four-momentum is defined from its decay products: $p_\mu^W = p_\mu^\ell + p_\mu^\gamma$.

by about 80% to $\sigma_{\text{incl}}^{\text{NLO}} = 131 \text{ fb}$) the jets tend to balance each other at small rapidity gaps of order one. These gaps are due to the dominant qg - and $\bar{q}g$ -induced partonic subprocesses of the dijet contribution. Due to the relatively large available phase space for additional jet emission, the corrections are particularly large for this phase space region, $K = 1.6$. This is in accordance with the large differential K factor around $\phi_{W\gamma} \lesssim \pi$ in Fig. 8. Note that this is also a part of the phase space which is more sensitive to the distinct photon isolation scales. In addition, with W and photon back-to-back, events with $|\phi_{W\gamma}| \geq 150$ deg can be understood as “genuine” $pp \rightarrow W\gamma + X$ events, subject to anomalous couplings’ studies^{||}.

Anomalous couplings generically modify the p_T^γ distribution at large values, Eq. (10). It is therefore worth commenting on the impact of the NLO corrections onto the region of phase space characterized by very large p_T^γ already at this point. Considering energetic events in the tails of the p_T distributions (e.g. $p_T^\gamma > 1 \text{ TeV}$) the picture is quite different from the situation we have described above. Jet emission is logarithmically enhanced in the

^{||}These configurations give rise to large momentum transfers in the trilinear $WW\gamma$ coupling. The QCD corrections are therefore important to understand the deviations that result from anomalous couplings. We will discuss this in more detail in Sec. 3.4.

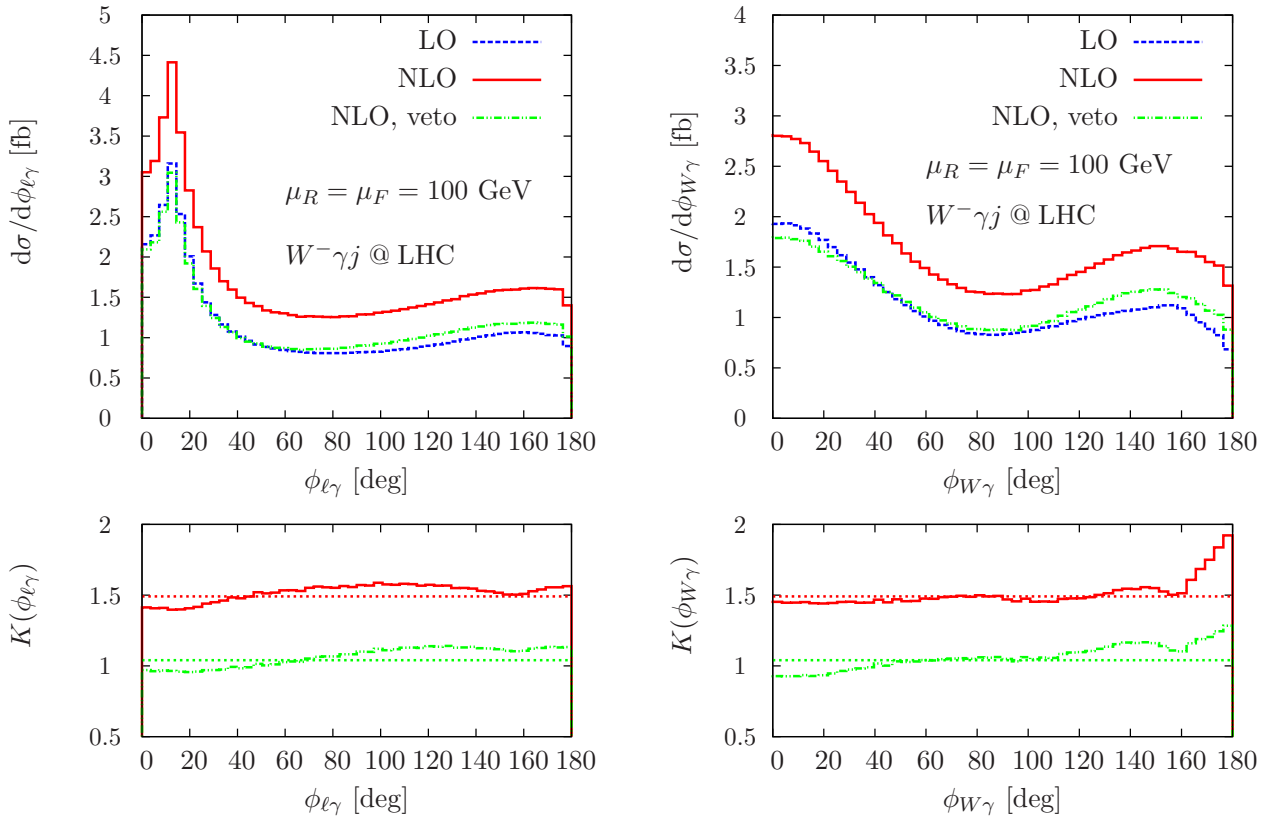


Figure 8: Leading order and next-to-leading order distributions of the azimuthal angle between photon and lepton, and photon and W . The horizontal lines display the K factors of the total inclusive and exclusive production.

dominant gluon-induced subprocesses $qg \rightarrow W\gamma Q$ already at LO, which can easily be seen from the Altarelli-Parisi [38] approximation of collinear emission $q \rightarrow QW$ as demonstrated in Ref. [11]

$$d\sigma(qg \rightarrow W\gamma Q) = d\sigma(qg \rightarrow q\gamma) \frac{e^2}{16\pi^2 \sin^2 \theta_w} \log^2 \frac{p_T^\gamma}{m_W^2}, \quad (20)$$

for a diagonal CKM matrix. The preferred situation is therefore a collinear W -jet pair that recoils against the hard photon. This region of phase space receives sizable QCD corrections: The extra parton emission in these events has no preferred direction in the azimuthal angle and is kinematically unsuppressed. The p_T^W distribution receives sizable corrections for the same reason. The uncertainties in this region of phase space are dominated by the dijet contribution, which is only determined to LO approximation in our calculation. Hence, our NLO correction does not improve the cross sections' stability in this extreme region of phase space. However, as the anomalous couplings affect the p_T^γ distribution at values much lower than $\Lambda \sim \text{TeV}$, see Eq. (10), the NLO corrections give rise to perturbatively predictive deviations from the SM, see Sec. 3.4.

Vetoing the second resolved jet, Eq. (18), removes most of the characteristics of additional

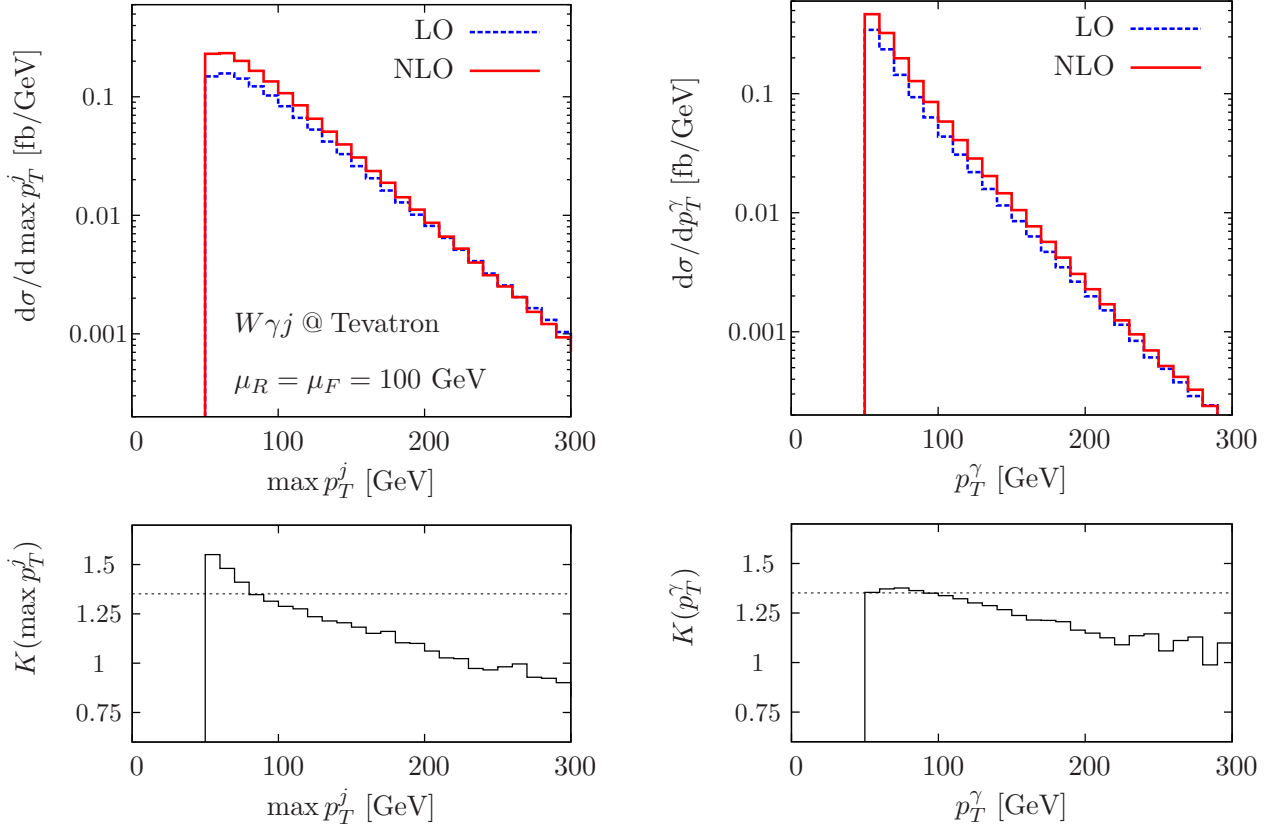


Figure 9: Leading order and next-to-leading order $\max(p_T^j)$ and p_T^γ distributions at the Tevatron, including the respective differential K factors. The horizontal line represents the K factor of the total inclusive production.

jet radiation. The total exclusive cross sections are tabulated in Tab. 2. Comparing the uncertainty band of the photon transverse momentum in Fig. 5 and the respective phase space dependence of the QCD corrections in Fig. 4, we conclude that perturbative stability against variations of factorization and renormalization scales of dijet-vetoed $pp \rightarrow \ell\nu\gamma j + X$ production shows up as a subtraction of a $\mathcal{O}(\alpha^3\alpha_s^2)$ leading-order contribution (the real emission dijet contribution) from a relatively stable inclusive NLO prediction. The vetoed contribution is kinematically well-accessible and unsuppressed by QCD dynamics. The larger scale dependence of the vetoed distributions' tails compared to inclusive production remains as an echo. At larger values of p_T^γ , exclusive production does not yield a perturbatively reliable result, which is also indicated by negative weights.

3.3 NLO QCD $W\gamma j$ production in the SM at the Tevatron

For Tevatron collisions we find a total cross section of

$$\sigma^{\text{NLO}} = (14.86 \pm 0.03) \text{ fb} \quad (K = 1.35). \quad (21)$$

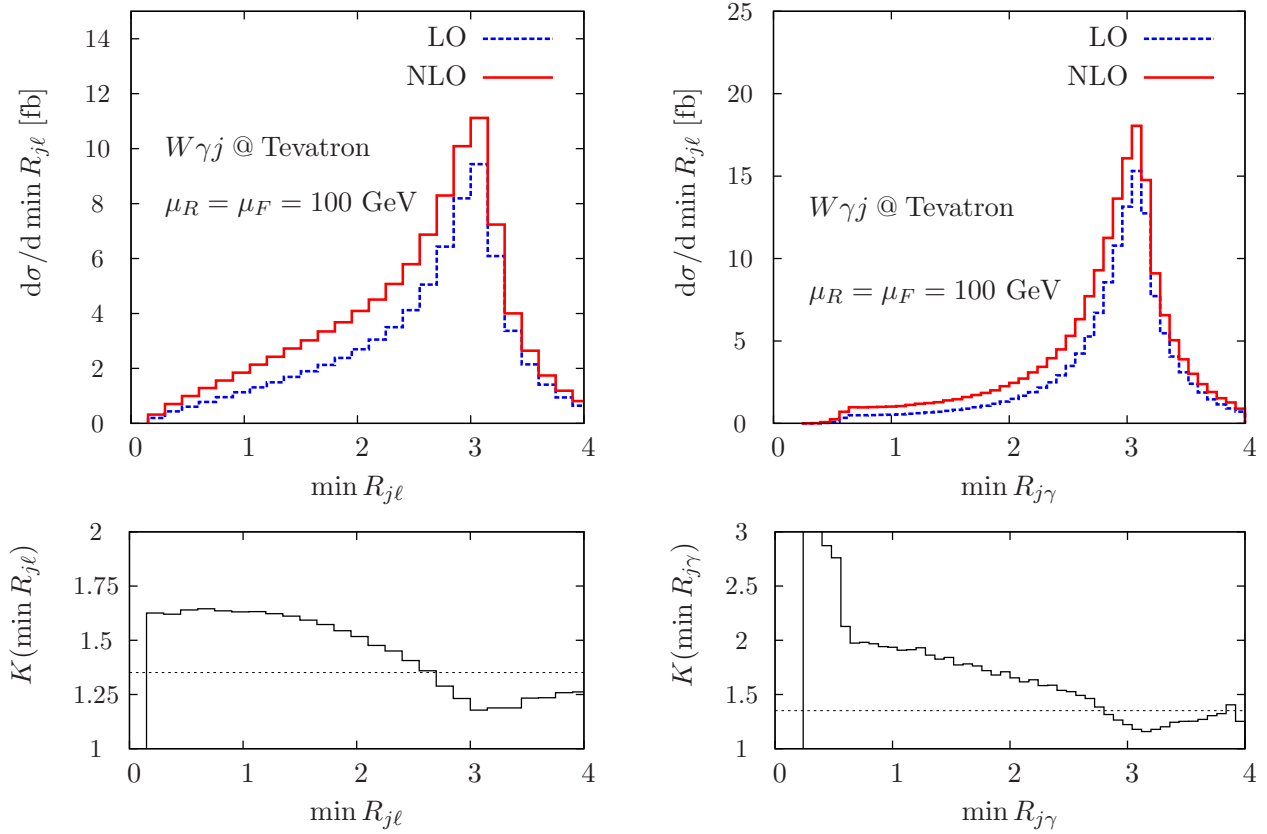


Figure 10: Leading order and next-to-leading order $\min R_{j\ell}$ and $\min R_{j\gamma}$ distributions at the Tevatron, including the respective differential K factors. The horizontal line gives the K factor of the total inclusive production.

The proton and the antiproton are tested at $x \sim 0.2$ so that $q\bar{Q}$ -induced subprocesses dominate the total hadronic cross section. The considerably lower center-of-mass energy compared to the LHC in combination with the cuts on the jet transverse momentum effectively introduces a jet veto, so that the Tevatron shapes resemble the NLO exclusive LHC distributions. The shapes of the transverse momentum distributions at large p_T are overestimated by the LO approximation, yielding differential K factors of order 0.5 at NLO for the distributions' tails. Since additional jet radiation is kinematically suppressed compared to the LHC, the semi-hadronic observables typically receive smaller relative corrections around the $\sigma^{\text{NLO}}/\sigma^{\text{LO}}$ rescaled LO distributions. Yet, QCD-radiation effects are still sizable, and events tend to be re-distributed to smaller minimum separations of the hadronic jets with respect to the lepton and the photon, Fig. 10.

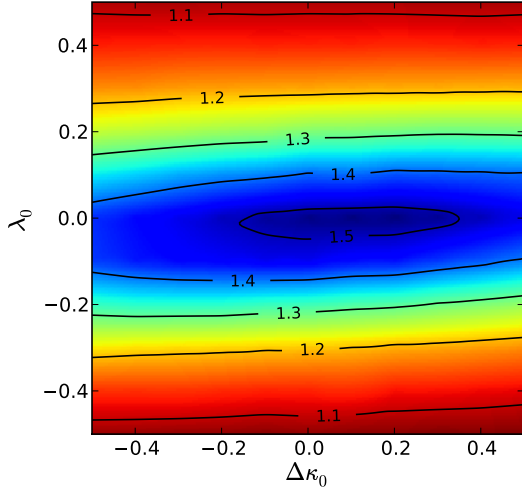


Figure 11: Total K factor contours for $pp \rightarrow e^-\bar{\nu}_e\gamma j + X$ cross section at the LHC for anomalous input parameters $|\Delta\kappa_0|, |\lambda_0| \leq 0.5$ with dipole form factor $n = 2$ and the cutoff scale $\Lambda = 1$ TeV.

3.4 NLO QCD $W\gamma$ +jet production with anomalous $WW\gamma$ couplings at the LHC

We now include anomalous couplings to the NLO $W\gamma$ + jet cross section predictions. Most stringent bounds on anomalous $WW\gamma$ couplings are currently given by the combined analysis of LEP data of Ref. [17],

$$1 + \Delta\kappa_0 = 0.984^{+0.042}_{-0.047}, \quad \lambda_0 = -0.016^{+0.021}_{-0.023}, \quad (22a)$$

and recent fits at hadron colliders are from the Tevatron D \emptyset experiment Ref. [18]

$$1 + \Delta\kappa_0 = 1.07^{+0.16}_{-0.20} \quad \lambda_0 = -0.0^{+0.05}_{-0.04}. \quad (22b)$$

Both bounds are at 68% confidence level, extracted from data assuming $\Lambda = 2$ TeV and dipole profiles. Note, that both experiments are consistent with the SM prediction $\Delta\kappa_0 = \lambda_0 = 0$. Generically, these bounds select a region in the parameter space where the QCD corrections are particularly important. This can be inferred from a scan over a wide (and experimentally ruled-out) range of anomalous parameters in Fig. 11. We choose cuts in resemblance to the selection criteria that are typically applied by the ATLAS collaboration to probe anomalous trilinear couplings, e.g., Ref. [10]

$$p_T^\gamma \geq 100 \text{ GeV}, \quad p_T^\ell, \not{p}_T \geq 25 \text{ GeV}, \quad R_{\ell\gamma} \geq 1.0, \quad (23)$$

where \not{p}_T denotes the missing transverse momentum. In addition, we choose inclusive hadronic jet cuts

$$p_T^j \geq 20 \text{ GeV}, \quad \delta_0 = 0.4, \quad R_{j\ell} \geq 0.2. \quad (24)$$

These cuts yield a too low total rate at the Tevatron to be phenomenologically important. This can also be inferred from comparing the p_T^γ distributions at the LHC and the Tevatron

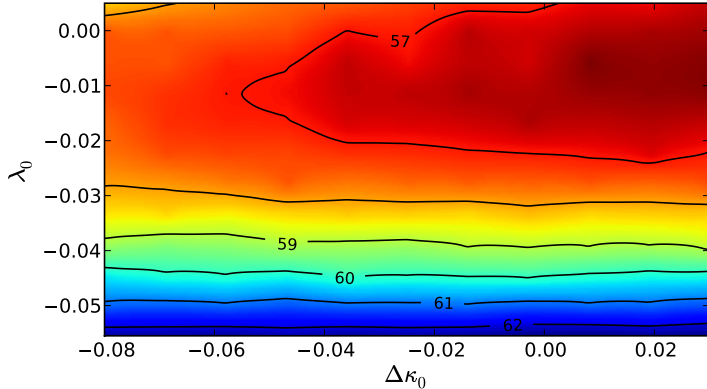


Figure 12: Inclusive NLO QCD $pp \rightarrow e^- \bar{\nu}_e \gamma j + X$ cross section contours at the LHC in fb after applying the cut of Eq. (3.15). We show the $W^- \gamma + \text{jet}$ cross section for parameters κ_0, λ_0 that are consistent with the LEP bounds. We choose dipole form factors $n = 2$ and a cutoff scale $\Lambda = 2$ TeV [10, 18].

for large values, where the effects of anomalous couplings will be visible, Figs. 5 and 9. We therefore focus on anomalous couplings at the LHC. The qualitative reason why the QCD corrections turn out large for parameter choices in the vicinity of the SM is easily uncovered by examining the corrections' p_T^γ dependence. From Fig. 4 we infer** that $K(p_T^\gamma) > K$ in the threshold region and $K(p_T^\gamma) < K$ in the tail of the distribution. Consequently, the region of phase space, where the anomalous couplings' impact is well-pronounced, i.e. $p_T^\gamma \lesssim \Lambda$, provides a smaller fraction to the NLO cross section for inclusive cuts compared to the LO approximation rescaled by the total K factor of inclusive production. Additionally, at low transverse momenta, the distributions are dominated by SM physics due to small momentum transfers in Eq. (10), so that they are largely independent of $\Delta\kappa_0, \lambda_0$ in this particular phase space region. In total, not only a large fraction of the cross section, but also a large share of its increase compared to LO, is insensitive to the underlying anomalous parameters for experimentally allowed values $\Delta\kappa_0, \lambda_0$. This is completely analogous to anomalous $WZ + \text{jet}$ production [9]. The NLO inclusive cross section is therefore less sensitive to the anomalous couplings than the LO cross section, and $K = \sigma^{\text{NLO}}/\sigma^{\text{LO}}$ is large in regions, where the distributions are dominated by their low p_T behavior: K peaks around the SM, $\Delta\kappa = \lambda = 0$, Fig. 11. From Fig. 5 and the related discussion, it is also apparent that, in addition to lost perturbative stability for large p_T^γ , the effects of anomalous couplings are suppressed in exclusive $W\gamma + \text{jet}$ production.

To increase the sensitivity to κ_0 and λ_0 in the experimentally allowed range, we additionally require the W and the photon to be back-to-back in the transverse plane, by imposing an azimuthal angle

$$|\phi_{W\gamma}| \geq 150 \text{ deg}. \quad (25)$$

**We slightly abuse the notation: $K(p_T^\gamma)$ is the differential K factor in the sense of Eq. (19) and K without parentheses refers to the total K factor of exclusive production.

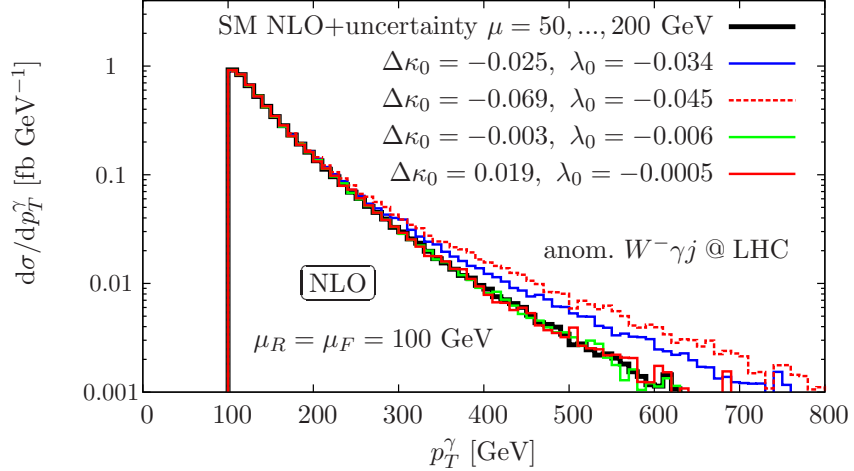


Figure 13: Inclusive NLO QCD distributions of the photon transverse momentum in anomalous $pp \rightarrow e^-\bar{\nu}_e\gamma j + X$ at the LHC for different parameters κ_0, λ_0 that are consistent with the LEP bounds. We choose dipole form factors $n = 2$ and a cutoff scale $\Lambda = 2$ TeV [10, 18]. The width of the SM curve represents the SM scale uncertainty that results from varying $\mu_R = \mu_F$ around the central scale of 100 GeV by a factor two.

This cut effectively mimics “genuine” $W\gamma$ events with additional hadronic activity. Given the hard p_T requirements, this selection criterion can be replaced by a cut on $|\phi_{\ell\gamma}|$ or $\Delta R_{\ell\gamma}$ without qualitatively changing the phenomenology (see also Figs. 7 and 8). The resulting variation of the integrated $W^-\gamma + \text{jet}$ cross section for parameters $(\Delta\kappa_0, \lambda_0)$ in the range of Eq. (22) is of order 10%, Fig. 12. Comparing this variation to the uncertainty inherent to the SM expectation at the given order of perturbation theory, which, e.g., yields $\sigma \simeq 60.6$ fb for $\mu_R = \mu_F = 50$ GeV, we see that the cross sections’ increase due to the anomalous couplings is compatible with the SM NLO scale uncertainty, signaling a vanishing sensitivity of the total rate to $\Delta\kappa_0, \lambda_0$.

This, however, does not hold for differential distributions at large momentum transfers, e.g. for the p_T^γ spectrum, which receives large anomalous couplings-induced modifications of the distribution’s tail. The altered spectrum is well outside the SM-uncertainty band for larger values of $(\Delta\kappa_0, \lambda_0)$, with a particular sensitivity to λ_0 . Remember that λ_0 dials the dimension six operator in Eq. (8), which is not present in the SM. The characteristic enhancement vanishes when the anomalous parameters approach their SM values, and the shape deviations become comparable to the distribution’s uncertainty. The larger cross section at large p_T^γ compared to the SM translates into an increased cross section for the $W\gamma$ back-to-back configurations, which is also visible in the pseudorapidity differences at small separation, Fig. 14. The anomalous couplings’ impact on this distribution is qualitatively different from the QCD corrections, which exhibit $K(p_T^\gamma) < K$ for large p_T^γ . Therefore, the NLO cross section at small rapidity differences is smaller than the NLO-normalized LO distributions suggests, Fig. 7. Yet, the NLO uncertainty from integrating over the small p_T configurations cover the anomalous couplings effect entirely, already by varying the scale within a small interval, as indicated in Fig. 14. Given the residual anomalous couplings-

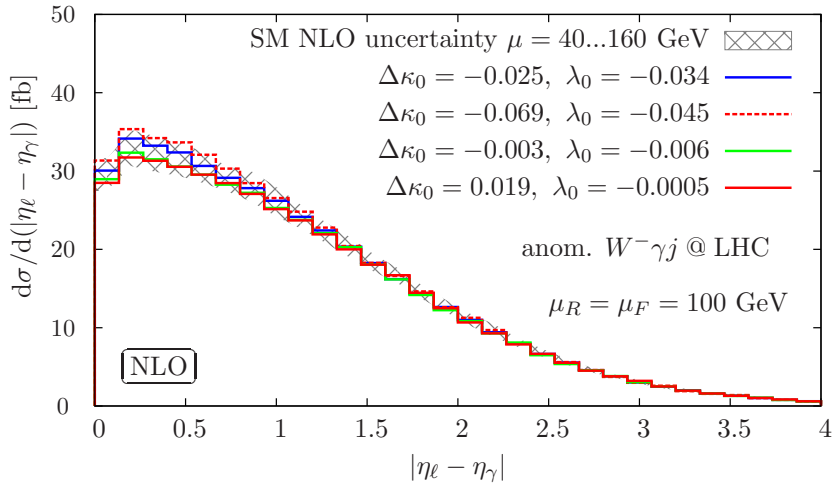


Figure 14: Inclusive NLO QCD distributions of the photon lepton rapidity difference in anomalous $pp \rightarrow e^- \bar{\nu}_e \gamma j + X$ at the LHC. We show histograms with different parameters κ_0, λ_0 that are consistent with the LEP bounds. We choose dipole form factors $n = 2$ and a cutoff scale $\Lambda = 2$ TeV [10, 18].

induced deviations of the p_T^γ shape, a more inclusive measurement strategy that relies on fits to the inclusive p_T^γ spectrum or on multivariate analysis of the distributions can supplement traditional techniques and appears to be practicable. This is also motivated by the overall theoretical uncertainty of order 10% becoming comparable to the estimated experiments' systematics at the reported order of perturbation theory.

4 Summary and Conclusions

In this paper, we have calculated the differential NLO QCD corrections to $W\gamma$ production in association with a hadronic jet, including full leptonic decays and all off-shell effects of the W . We have given details on the calculation's strategy and have also discussed the effects of anomalous $WW\gamma$ couplings. The corrections are sizable and exhibit substantial phase space dependencies, and should be included in phenomenological analysis which employ these processes, either as signal or as background. In particular, we have found the exclusive production's perturbative stability to be accidental — additional jet vetoing does not amount to a experimental strategy which is under good theoretical control at the given order of perturbation theory. Qualitatively identical results have been shown to hold for $WZ +$ jet production in Ref. [8], where the dominant QCD corrections are identical and only get tested at different scales. This strongly indicates that the additional jet veto does not provide a meaningful procedure for the entire class of massive diboson plus jet cross sections beyond theoretical contemplation.

Even if theoretically less favored due to kinematical obstruction, inclusive $W\gamma +$ jet production (and hence inclusive $W\gamma$ production) exhibits potential sensitivity to anomalous

couplings via shape deviations of the p_T^γ distribution. Integrated cross sections for our inclusively chosen leptonic cuts, however, entirely loose their sensitivity to modifications of the electroweak sector due to the low- p_T QCD uncertainties. Providing the NLO corrections to $pp \rightarrow \ell^\pm + \gamma + \not{p}_T + \text{jet} + X$, we realistically asses the impact of anomalous couplings on the characteristic p_T^γ distribution in Fig. 13. For larger anomalous couplings that are still compatible with the combined LEP measurements, the distributions significantly deviate from their SM expectation and fall well outside the SM distribution's uncertainty. Comparing to anomalous $WZ + \text{jet}$ production, we find more sizable deviations in the distributions' shapes in the allowed parameter range. Whether the observed sensitivity can be carried over to the experiment represents a challenging question, which is beyond the scope of this work. We leave a more thorough investigation of this direction to future work.

Acknowledgements

We thank Dieter Zeppenfeld for collaboration during the initial stage of this work. We also thank Steffen Schumann for SHERPA-support. F.C acknowledges partial support by FEDER and Spanish MICINN under grant FPA2008-02878. C.E. is supported in parts by the Karlsruhe Graduiertenkolleg “High Energy Particle and Particle Astrophysics”. This research is partly funded by the Deutsche Forschungsgemeinschaft under SFB TR-9 “Computergestützte Theoretische Teilchenphysik”, and the Helmholtz alliance “Physics at the Terascale”.

References

- [1] J. Ohnemus, Phys. Rev. D **44** (1991) 1403, J. Ohnemus, Phys. Rev. D **44** (1991) 3477, J. Ohnemus, Phys. Rev. D **47** (1993) 940, J. Ohnemus, arXiv:hep-ph/9503389.
- [2] S. Dittmaier, S. Kallweit and P. Uwer, Phys. Rev. Lett. **100**, 062003 (2008).
- [3] J. M. Campbell, R. Keith Ellis and G. Zanderighi, JHEP **0712** (2007) 056.
- [4] S. Dittmaier, S. Kallweit and P. Uwer, Nucl. Phys. B **826**, 18 (2010).
- [5] F. Campanario, C. Englert, M. Spannowsky and D. Zeppenfeld, Europhys. Lett. **88**, 11001 (2009).
- [6] T. Binoth, T. Gleisberg, S. Karg, N. Kauer and G. Sanguinetti, Phys. Lett. B **683** (2010) 154.
- [7] S. Ji-Juan, M. Wen-Gan, Z. Ren-You and G. Lei, Phys. Rev. D **81** (2010) 114037.
- [8] F. Campanario, C. Englert, S. Kallweit, M. Spannowsky and D. Zeppenfeld, JHEP **1007** (2010) 076.
- [9] F. Campanario, C. Englert and M. Spannowsky, Phys. Rev. D **82** (2010) 054015.

- [10] M. Dobbs, AIP Conf. Proc. **753**, 181 (2005).
- [11] U. Baur, T. Han and J. Ohnemus, Phys. Rev. D **48** (1993) 5140.
- [12] L. J. Dixon, Z. Kunszt and A. Signer, Phys. Rev. D **60** (1999) 114037.
- [13] F. K. Diakonos, O. Korakianitis, C. G. Papadopoulos, C. Philippides and W. J. Stirling, Phys. Lett. B **303** (1993) 177.
- [14] E. Chapon, C. Royon and O. Kepka, Phys. Rev. D **81** (2010) 074003.
- [15] D. Levin [ATLAS Collaboration], ATL-COM-PHYS-2008-179.
- [16] T. Müller, D. Neuberg, and W. Thümmel, CERN-CMS-NOTE-2000-017 (2000).
- [17] J. Alcaraz *et al.* [ALEPH Collaboration and DELPHI Collaboration and L3 Collaboration and OPAL Collaboration and LEP Electroweak Working Group], [arXiv:hep-ex/0612034](https://arxiv.org/abs/hep-ex/0612034).
- [18] V. M. Abazov *et al.* [D \emptyset Collaboration], Phys. Rev. Lett. **100** (2008) 241805; V. M. Abazov *et al.* [D \emptyset Collaboration], [arXiv:0907.4952](https://arxiv.org/abs/0907.4952).
- [19] R. W. Brown, K. L. Kowalski and S. J. Brodsky, Phys. Rev. D **28** (1983) 624.
- [20] P. Fisher, U. Becker and J. Kirkby, Phys. Lett. B **356** (1995) 404; U. Baur, S. Keller and W. K. Sakumoto, Phys. Rev. D **57** (1998) 199.
- [21] K. Arnold *et al.*, Comput. Phys. Commun. **180** (2009) 1661.
- [22] H. Murayama, I. Watanabe and K. Hagiwara, KEK-Report 91-11, 1992.
- [23] J. Alwall *et al.*, JHEP **0709** (2007) 028.
- [24] G. P. Lepage, J. Comput. Phys. **27** (1978) 192.
- [25] T. Gleisberg, S. Hoche, F. Krauss, M. Schonherr, S. Schumann, F. Siegert and J. Winter, JHEP **0902** (2009) 007.
- [26] A. Denner, S. Dittmaier, M. Roth, and D. Wackerlo, Nucl. Phys. B **560** (1999), 33; C. Oleari and D. Zeppenfeld, Phys. Rev. D **69** (2004), 093004.
- [27] A. van Hameren, J. Vollinga and S. Weinzierl, Eur. Phys. J. C **41** (2005) 361.
- [28] A. Bredenstein, A. Denner, S. Dittmaier and S. Pozzorini, JHEP **0808** (2008) 108.
- [29] G. Passarino and M. J. G. Veltman, Nucl. Phys. B **160**, 151 (1979).
- [30] A. Denner and S. Dittmaier, Nucl. Phys. B **658** (2003) 175, A. Denner and S. Dittmaier, Nucl. Phys. B **734** (2006) 62.

- [31] G. Bozzi, B. Jager, C. Oleari and D. Zeppenfeld, Phys. Rev. D **75** (2007) 073004; V. Hankele and D. Zeppenfeld, Phys. Lett. B **661** (2008) 103; F. Campanario, V. Hankele, C. Oleari, S. Prestel and D. Zeppenfeld, Phys. Rev. D **78** (2008) 094012; C. Englert, B. Jager and D. Zeppenfeld, JHEP **0903** (2009) 060; G. Bozzi, F. Campanario, V. Hankele and D. Zeppenfeld, Phys. Rev. D **81** (2010) 094030; K. Arnold, T. Figy, B. Jager and D. Zeppenfeld, JHEP **1008** (2010) 088.
- [32] T. Hahn, Comput. Phys. Commun. **140** (2001) 418.
- [33] R. Mertig, M. Bohm and A. Denner, Comput. Phys. Commun. **64** (1991) 345.
- [34] K. Hagiwara and D. Zeppenfeld, Nucl. Phys. B **313** (1989) 560.
- [35] S. Catani and M. H. Seymour, Nucl. Phys. B **485** (1997) 291 [Erratum-ibid. B **510** (1998) 503].
- [36] R. Frederix, T. Gehrmann and N. Greiner, JHEP **0809** (2008) 122.
- [37] G. Aad *et al.* [ATLAS Collaboration], JINST **3** (2008) S08003, G. L. Bayatian *et al.* [CMS Collaboration], J. Phys. G **34** (2007) 995.
- [38] V. N. Gribov and L. N. Lipatov, Sov. J. Nucl. Phys. **15** (1972) 438 [Yad. Fiz. **15** (1972) 781]; G. Altarelli and G. Parisi, Nucl. Phys. B **126** (1977) 298; Y. L. Dokshitzer, Sov. Phys. JETP **46** (1977) 641.
- [39] T. Figy, C. Oleari and D. Zeppenfeld, Phys. Rev. D **68** (2003) 073005, C. Oleari and D. Zeppenfeld, Phys. Rev. D **69** (2004) 093004.
- [40] T. Figy, V. Hankele and D. Zeppenfeld, JHEP **0802** (2008) 076.
- [41] K. Hagiwara, R. D. Peccei, D. Zeppenfeld and K. Hikasa, Nucl. Phys. B **282** (1987) 253.
- [42] U. Baur and D. Zeppenfeld, Phys. Lett. B **201** (1988) 383.
- [43] C. Amsler *et al.* [Particle Data Group], Phys. Lett. B **667** (2008) 1.
- [44] N. D. Christensen and C. Duhr, Comput. Phys. Commun. **180** (2009) 1614.
- [45] J. Pumplin, D. R. Stump, J. Huston, H. L. Lai, P. Nadolsky, and W. K. Tung, JHEP **0207** (2002), 012.
- [46] S. Catani, Y. L. Dokshitzer, M. H. Seymour, and B. R. Webber, Nucl. Phys. B **406** (1993), 187, S. D. Ellis and D. E. Soper, Phys. Rev. D **48** (1993) 3160.
- [47] S. Frixione, Phys. Lett. B **429** (1998) 369.
- [48] M. Escalier, F. Derue, L. Fayard, M. Kado, B. Laforge, C. Reifen, and G. Unal, CERN-ATL-PHYS-PUB-2005-018